SUBSONIC AND TRANSONIC WIND TUNNEL TESTING OF TWO INFLATABLE AERODYNAMIC DECELERATORS

Christopher L. Tanner[(1)], Juan R. Cruz[(2)], Monica F. Hughes[(3)], Ian G. Clark[(4)], Robert D. Braun[(5)]

[(1)]Georgia Institute of Technology, Atlanta, Georgia 30332-0150 USA, Email: christopher.tanner@gatech.edu
[(2)]NASA Langley Research Center, Hampton, Virginia 23681-2199 USA, Email: juan.r.cruz@nasa.gov
[(3)]NASA Langley Research Center, Hampton, Virginia 23681-2199 USA, Email: monica.f.hughes@nasa.gov
[(4)]Georgia Institute of Technology, Atlanta, Georgia 30332-0150 USA, Email: ian.clark@ae.gatech.edu
[(5)]Georgia Institute of Technology, Atlanta, Georgia 30332-0150 USA, Email: robert.braun@ae.gatech.edu

ABSTRACT

Two inflatable aerodynamic decelerator designs were tested in the Transonic Dynamics Tunnel at the NASA Langley Research Center: a tension cone and an isotensoid. The tension cone consists of a flexible tension shell attached to a torus and the isotensoid employs a ram-air inflated envelope. Tests were conducted at Mach numbers from 0.3 to 1.08 and Reynolds numbers from 0.59 to 2.46 million. The main objective of these tests was to obtain static aerodynamic coefficients at subsonic and transonic speeds to supplement supersonic aerodynamic data for these same two designs. The axial force coefficients of both designs increased smoothly from subsonic through transonic Mach numbers. Dynamic data show significant oscillation of the tension cone and minimal oscillation of the isotensoid. The transonic and subsonic data will be used to assemble an inflatable decelerator aerodynamic database for use in computational analyses and system studies.

1. INTRODUCTION

Supersonic inflatable aerodynamic decelerators (IADs) represent an alternate technology to supersonic parachutes for deceleration in thin atmospheres, particularly at Mars. Supersonic IADs are inflated after peak heating at Mach numbers less than five and decelerate the entry vehicle to subsonic speeds. The 2011 Mars Science Laboratory (MSL) mission is pushing the qualification limits of the disk-gap-band (DGB) parachute [1] established by the Viking program in the late 1960's by deploying the parachute at Mach 2.2 [2]. Re-qualifying the DGB parachute for missions with landed mass greater than MSL would likely provide only marginal performance enhancements. In contrast, development and qualification of supersonic IADs may provide a means of increasing the entry vehicle's drag area at Mach numbers and dynamic pressures well above those achievable by supersonic parachutes.

A recent resurgence of interest in inflatable decelerator technology has prompted further investigation into two supersonic IAD designs: the tension cone and the isotensoid. Analyses of these two shapes highlight several system-level benefits that enable increased landed mass and higher landing altitudes on Mars for large robotic missions [2]. Supersonic wind tunnel tests were recently performed on tension cone models [3,4] to quantify their aerodynamic performance and provide data for comparison against the supersonic aerodynamic performance of isotensoid models [5,6]. Results from these wind tunnel tests show good static aerodynamic performance and rapid, stable deployments in supersonic flow for both the tension cone and isotensoid.

The subsonic and transonic aerodynamic behavior of both IAD designs is important for their viability. In particular, the stability of IADs in subsonic flight is a critical metric for ground acquisition and lander separation events. Additionally, subsonic and transonic drag characteristics must be quantified to determine a terminal descent velocity, which is a critical design parameter for the final descent system. However, most experimentation up to this point has focused on the IAD's supersonic characteristics. This paper presents preliminary partial results for subsonic and transonic tests performed on flexible IAD models. These data include static aerodynamic performance of both IAD designs as well as data regarding their static and dynamic aeroelastic behavior.

2. TRANSONIC DYNAMICS TUNNEL

Subsonic and transonic wind tunnel testing took place in the Transonic Dynamics Tunnel (TDT), located at the NASA Langley Research Center (LaRC) in Hampton, Virginia, USA. The TDT features a 4.9x4.9-m (16x16-ft) test section with slotted walls to allow for transonic operations. The test section is show in Fig. 1

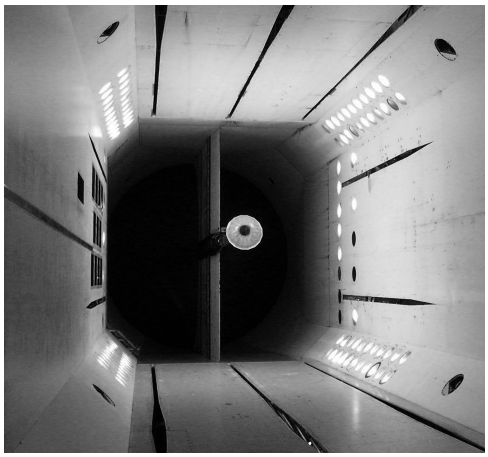

Fig. 1. TDT test section with slotted walls. Tension cone model is seen mounted on the centerline sting.

The tunnel is capable of operation at Mach numbers ranging from near zero to 1.20*. To achieve a wide range of Reynolds numbers, the tunnel can be operated in sub-atmospheric conditions, reaching a minimum total pressure of approximately 1400 Pa. All transonic and subsonic tests reported in this paper were conducted at sub-atmospheric pressures in air.

Aerodynamic forces and moments were measured using a six-axis strain gauge balance. High-resolution photographs were taken using a twelve mega-pixel camera. Video data were taken at thirty frames per second (fps) from three camera angles and at 100 fps from one camera angle. Photogrammetry data were obtained using a four-camera system, but these results are not reported in this paper.

3. TENSION CONE

Fig. 2. Tension cone attached to an entry vehicle.

3.1. Geometry

The tension cone IAD, shown in Fig. 2, consists of an axisymmetric single-surface tension shell that is designed to carry only tensile stresses in the meridional and circumferential directions when aerodynamically loaded [7]. The tension shell is attached to an inflatable torus at its outer perimeter. Pressurization gas for the torus is supplied by an onboard pressure source such as a high-pressure tank or a gas generator.

* The upper Mach number quoted is for an empty test section.

3.2. Wind Tunnel Model Description

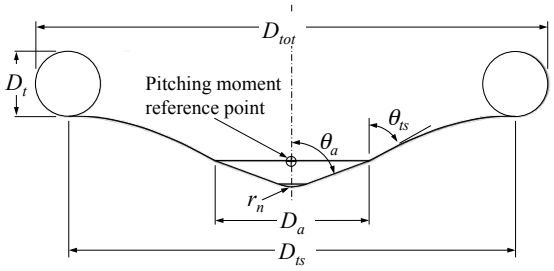

Fig. 3. Tension cone geometry.

The shape of the tension cone model was obtained assuming zero circumferential stress and using a supersonic pressure distribution calculated by inviscid computational fluid dynamic analyses. Model fabrication required the ideal axisymmetric shape to be approximated by a sixteen-sided polygon with the as-designed total diameter (D_{tot}) measured across the flats. The models consist of a rigid 70° sphere cone aeroshell and a flexible tension shell constructed from urethane-coated Kevlar®. Given that inflation dynamics are not of interest in the transonic regime, a rigid torus composed of aluminum, foam, and fiberglass was used in lieu of an inflatable torus. The rigid torus has a weight of approximately 26 N (6 lb). The model's principal dimensions, shown in Fig. 3, are given in Table 1 (a more detailed description of the model's geometry is found in [4]).

Table 1. Tension cone as-designed model dimensions.

Dimension	Symbol	Value (m)
Total diameter	D_{tot}	0.600
Torus diameter	D_t	0.0750
Tension shell diameter	D_{ts}	0.525
Tension shell half-cone angle	θ_{ts}	60°
Aeroshell diameter	D_a	0.184
Aeroshell nose radius	r_n	0.0474
Aeroshell half-cone angle	θ_a	70°
Burble fence diameter	D_b	0.00953

Two tension cone IAD models were tested in the TDT. One of them is the same model that was tested in the 3x3-m (10x10-ft) Supersonic Wind Tunnel at NASA Glenn Research Center [3,4]. A second model incorporates a 9.5-mm (3/8-inch) burble fence at approximately the torus's maximum diameter in an attempt to increase transonic and subsonic stability. The purpose of the burble fence is to force the flow to separate uniformly at the same location around the torus, enhancing stability. The two models are shown in Fig. 4 with and without a burble fence. The burble fence design was the result of a qualitative selection process performed at the 6.1-m (20-ft) Vertical Spin Tunnel at the NASA Langley Research Center prior

to starting the TDT test. The tension cone models tested in the TDT did not employ the anti-torque panels that were used on the models tested in the NASA Glenn Research Center Supersonic Wind Tunnel [3,4].

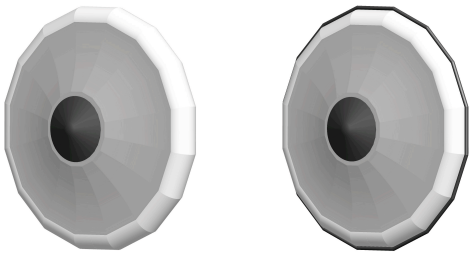

(a) Without burble fence (Model 1)

(b) With burble fence (Model 2)

Fig. 4. Tension cone models with and without burble fence.

3.3. Objectives and Test Conditions

The purpose of this test was to acquire data characterizing the static aerodynamic performance and aeroelastic behavior of the tension cone IAD in the subsonic and transonic flight regimes. Test conditions were designed to be representative of a relevant MSL-class entry and descent trajectory at Mars.

Tests were performed at Mach numbers ranging from 0.3 to 1.08 and Reynolds numbers ranging from 590 thousand (abbreviated 590K) to 2.5 million (abbreviated 2.5M) using the model's maximum diameter as the reference length. The maximum Mach number was limited by tunnel drive power and test section blockage. Tests were conducted at angles of attack from -5° to 15°. Both models used the same test matrix.

3.4. Static Aerodynamic Performance

Static aerodynamic coefficients were non-dimensionalized by the as-built projected area of the 16-sided polygon and as-built model total diameter given in Table 2. Note that the as-built dimensions of Model 1 vary slightly from the as-designed dimensions given in Table 1; this difference was due to manufacturing tolerances. The reference length and reference area of Model 2 include the burble fence.

Table 2. Tension cone reference dimensions.

	Reference Area, S_{ref} (m^2)	Reference Length, c_{ref} (m)
As-designed	$\pi D_{tot}^2/4$	D_{tot}
Model l as-built	0.289	0.603
Model 2 as-built	0.308	0.622

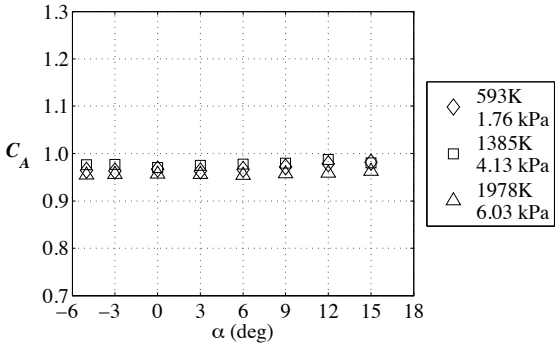

(a) Mach 0.60 for various Reynolds numbers and dynamic pressures

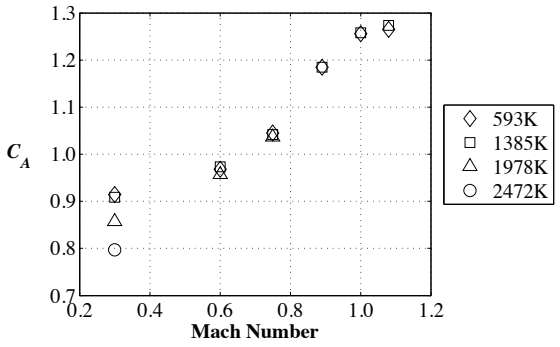

(b) 0° angle of attack for various Reynolds numbers

Fig. 5. Axial force coefficient (C_A) for tension cone Model 1.

The axial force coefficient of Model 1 is insensitive to Reynolds number, except at the lowest Mach number. At Mach 0.6 the axial force coefficient is nearly constant with angle of attack, as shown in Fig. 5(a). The axial force coefficient increases smoothly through the transonic region, which is distinctly different from the decrease in axial force observed for DGB parachutes in the transonic region [1].

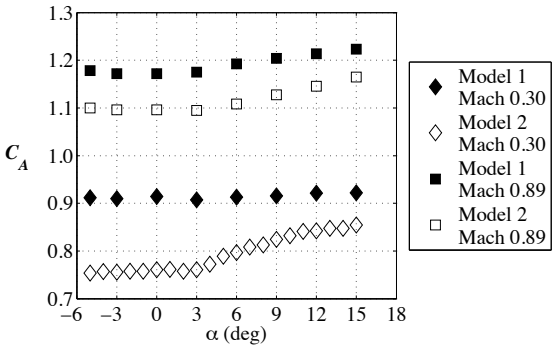

Fig. 6. Axial force coefficient comparison of tension cone Model 1 (filled symbols) and Model 2 (open symbols) at a Reynolds number 590K.

The introduction of a burble fence caused the axial force coefficient of Model 2 to be lower than Model 1, as shown in Fig. 6. This decrease is due to a small change in axial force but an increase in reference

area from the addition of the burble fence. Additionally, the axial force coefficient of Model 2 at Mach 0.3 increases at angles of attack greater than 3°, as compared to the nearly constant value of the axial force coefficient with respect to angle of attack for Model 1. Note that there is a slight asymmetry in the axial force coefficient for Model 2 at Mach 0.3 about the 0° angle of attack (compare the values of C_A for angles of attack ±5°). This effect is likely due to the weight of the torus, which causes the torus to pitch nose up and fly at a slight angle of attack with respect to the wind tunnel sting even though the mode angle of attack is 0°.

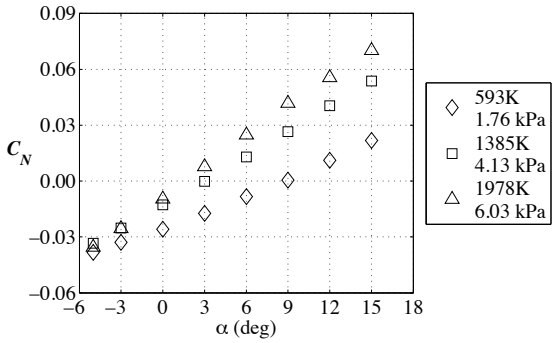

Fig. 7. Normal force coefficient (C_N) of tension cone, Model 1, at Mach 0.60 at various Reynolds numbers and dynamic pressures.

The normal force coefficient for Model 1 at Mach 0.6 and various Reynolds numbers is shown in Fig. 7. Reynolds number effects are greater in the normal direction than in the axial direction. Torus weight effects also manifest in the normal direction, causing a non-zero normal force coefficient at 0° angle of attack, as shown in Fig. 7. Normal force coefficient trends towards zero at 0° angle of attack as dynamic pressure increases.

Both Model 1 and Model 2 are statically stable when the pitching moment coefficient is taken about the reference point shown in Fig. 3. This reference point represents the approximate location of the center of mass for an MSL-class vehicle. Pitching moment coefficient is given in Fig. 8 versus angle of attack.

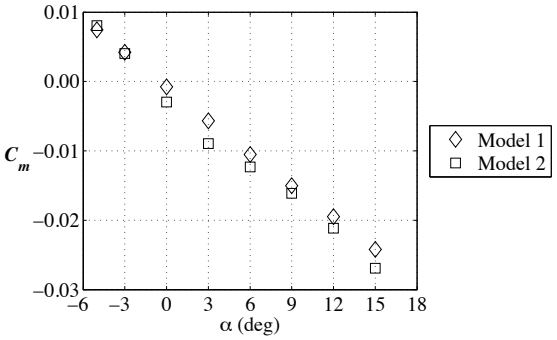

Fig. 8. Pitching moment coefficient (C_m) of tension cone about reference point at Mach 0.60, Re 1.4M, q 4.1 kPa.

3.5. Static Aeroelastic Behavior

Fig. 9 shows a comparison against the design shape of the static aeroelastic shape of the tension cone at subsonic and transonic speeds. Profile data were extracted from high-resolution images.

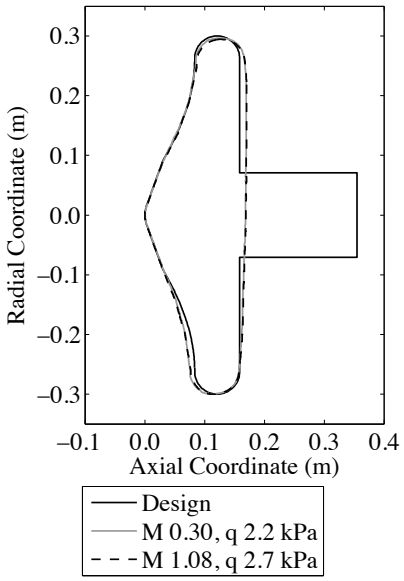

Fig. 9. Comparison of tension cone, Model 1, profiles at Re 1.4M.

The profiles at Mach 0.30 and Mach 1.08 match each other very closely despite the difference in Mach number. Additionally, both profiles match closely with the design shape. However, Fig. 9 shows a slight rotational offset between the TDT profiles and the design shape. This offset was discussed previously in Section 3.4 and is due to the weight of the torus. The torus angle measures approximately 0.7° with respect to the design shape. At angle of attack, the tension cone tends to remain mostly, but not exactly, aligned with the sting rather than aligning itself with the freestream flow as can be seen in Fig. 10. In Fig. 10(b) a slight negative pitch angle of the torus with respect to the sting can be noticed.

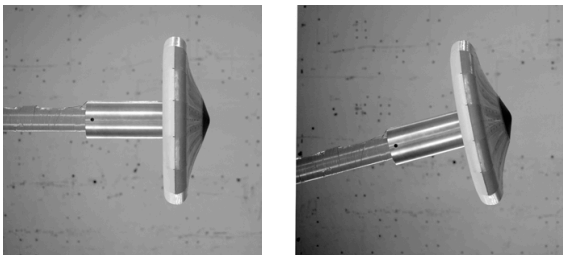

(a) 0° AoA (b) 9° AoA

Fig. 10. Tension cone, Model 1, orientation at angle of attack at Mach 0.75 and Re 2.0M.

3.6. Dynamic Behavior Observations

At 0° angle of attack, Model 1 exhibited relatively high-frequency oscillation in both the pitch and yaw axes at every test condition. The oscillations appeared to be multi-modal with amplitudes increasing with dynamic pressure. The tension cone appeared more stable at angle of attack.

Addition of a burble fence did not stabilize the observed oscillatory modes to the extent that had been hoped for. At 0° angle of attack, Model 2 exhibited oscillatory behavior similar to Model 1 with only slightly lower amplitudes. At angle of attack, Model 2 appeared to be more stable than Model 1.

Despite significant oscillation during testing, there were no visible signs of wear on the Kevlar® tension shell after several hours of testing.

4. ISOTENSOID

Fig. 11. Isotensoid attached to an entry vehicle.

4.1. Geometry

The isotensoid IAD, shown in Fig. 11, consists of an envelope designed to carry constant tension along meridian cords and uniform tensile stress in both the meridional and circumferential directions [8]. This type of IAD is typically inflated using ram-air pressure supplied via inlets located on the envelope.

4.2. Wind Tunnel Model Description

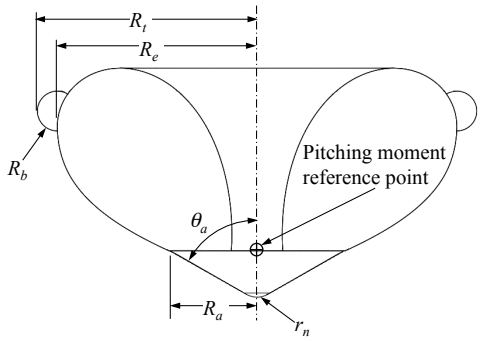

Fig. 12. Isotensoid geometry.

One goal for this test was to create a decelerator similar in shape to a model tested previously at supersonic speeds [6]. The subsonic and transonic data obtained during the present research would then supplement the available supersonic data [5,6]. The model was designed using the same non-dimensional profile coordinates specified in [9] and scaled to an equatorial radius approximately equal to the tension cone model. The as-designed dimensions shown in Fig. 12 are given in Table 3.

Table 3. Isotensoid as-designed model dimensions.

Dimension	Symbol	Value (m)
Total radius	R_t	0.330
Equatorial radius	R_e	0.300
Burble fence radius	R_b	0.030
Aeroshell radius	R_a	0.132
Aeroshell nose radius	r_n	0.0165
Aeroshell half-cone angle	θ_a	60°

Total, equatorial, and burble fence radii are specified at the meridian cords.

The model consists of a rigid 60° sphere cone aeroshell, and an isotensoid envelope with sixteen gores made of F-111 nylon fabric and sixteen meridians made of Vectran® cord. The stock F-111 fabric was given a thin coat of urethane, which decreased porosity to 0.003 cubic feet per minute per square foot of material at ½-inch of water pressure differential. A burble fence runs around the maximum diameter of the envelope and is constructed from the same coated F-111 fabric as the gores. The model is fully inflatable (envelope and burble fence) and features four ram-air inlets equally spaced around the decelerator just below the burble fence. Inlets are held open by rigid D-shaped rings and are held normal to the flow by Vectran® cords.

The model was designed as a sixteen-sided polygon with vertices at the meridian cords in which lobing (i.e., the curvature within each side of the polygon) was not specifically accounted for in the gore pattern.

The F-111 fabric elasticity allows some lobing to occur when the envelope is pressurized.

4.3. Objectives and Test Conditions

The objectives of this test were nearly identical to the objectives listed in Section 3.3 for the tension cone. In addition to acquiring aerodynamic and aeroelastic data, ram-air pressure recovery data were also obtained to investigate how the envelope's internal pressure responds to different test conditions. Test conditions for the isotensoid test were identical to the tension cone. Since the model diameter could not be measured in-situ, reference length is taken to be the design total diameter ($2R_t$).

4.4. Static Aerodynamic Performance

Static aerodynamic coefficients were non-dimensionalized using the as-designed projected area (0.347 m^2) as the reference area and as-designed model total diameter (0.660 m) as the reference length. Axial force coefficients are shown in Fig. 13.

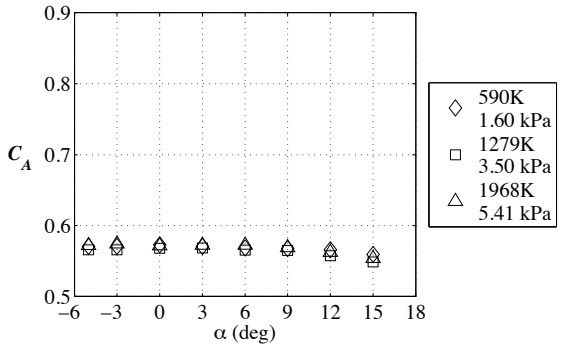

(a) Mach 0.60 for various Reynolds numbers and dynamic pressures.

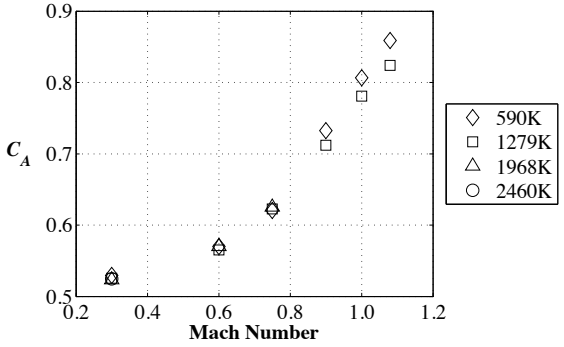

(b) 0° angle of attack for various Reynolds numbers.

Fig. 13. Axial force coefficient of isotensoid model.

Similar to the tension cone, the axial force coefficient of the isotensoid is nearly constant across this range of angles of attack. The axial force coefficient also increases continuously through the transonic region. However, the isotensoid has a significantly lower axial force coefficient than the tension cone at the same test condition due to its design shape, which is less blunt that the tension cone.

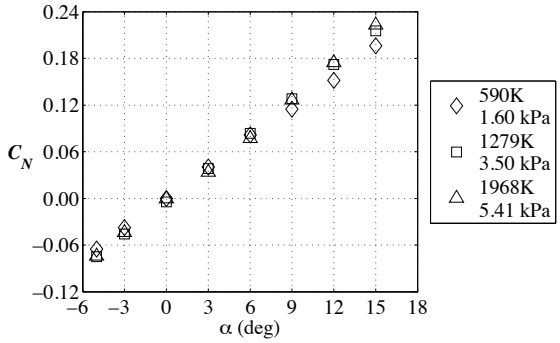

Fig. 14. Normal force coefficient of isotensoid model at Mach 0.60.

Fig. 14 shows that the isotensoid generates significantly greater normal force than the tension cone. Contrary to the tension cone, the isotensoid attempts to align itself with the freestream flow instead of remaining aligned with the wind tunnel sting when at angle of attack. Alignment of the isotensoid envelope with the flow is a significant contributor in this relatively large normal force coefficient. See section 4.5, Static Aeroelastic Behavior, for a discussion of the isotensoid deformation at angle of attack.

Fig. 15 illustrates static stability of the isotensoid design with the pitching moment at the reference point shown in Fig. 12, which corresponds to the approximate location of the center of mass for an MSL-class entry vehicle.

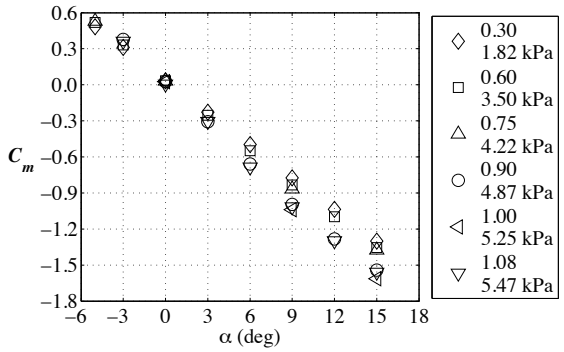

Fig. 15. Pitching moment coefficient about reference point at Re 1.28M.

The isotensoid's pitching moment slope is considerably more negative than the tension cone. This result must be interpreted carefully, however, as the isotensoid envelope contacted and imposed an asymmetric normal force on the measuring side of the sting adapter/balance at non-zero angle of attacks. This contact between the envelope and the

balance has two significant effects. First, the contact imparts a normal force behind the pitching moment reference point, which increases the magnitude of the pitching moment curve slope making it more negative. Contact with the sting adapter/balance also causes the envelope to take a different shape than the one that would be obtained if the isotensoid were attached to a free-flying vehicle.

Internal pressure for a ram-air device can be analyzed as a proportion of the freestream dynamic pressure (p_i/q_∞) and the freestream total pressure (p_i/p_0). Fig. 16 shows the isotensoid envelope pressure with respect to both dynamic and total pressure.

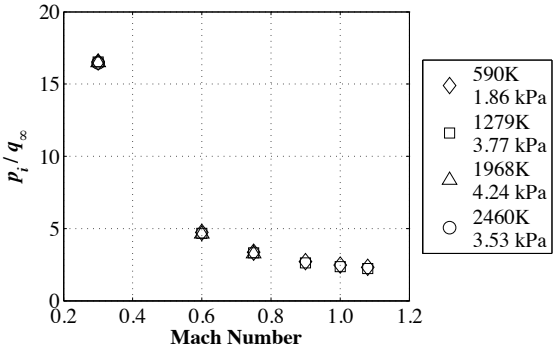

(a) Dynamic pressure recovery

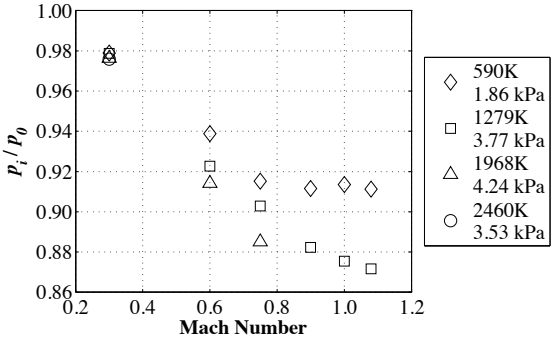

(b) Total pressure recovery

Fig. 16. Envelope internal pressure recovery at 0° angle of attack for various Reynolds numbers and dynamic pressures.

Total pressure recovery is highest for low Mach numbers, nearly 98%, and decreases nonlinearly with Mach number, achieving between 87% and 91% total pressure recovery at transonic speeds. Dynamic pressure recovery appears to asymptote to a value near $2q_\infty$, which is nearly identical to behavior observed during supersonic testing [6]. Fig. 16(b) shows some total pressure recovery sensitivity to Reynolds number, ranging by about 4% at transonic Mach numbers. A similar difference in recovery pressures is present in Fig. 16(a), but cannot be seen in this figure due to the scale of the p_i/q_∞ axis.

4.5. Static Aeroelastic Behavior

Fig. 17 shows a comparison of the static aeroelastic shape at transonic and subsonic speeds to the design shape. Profile data were extracted from high-resolution images.

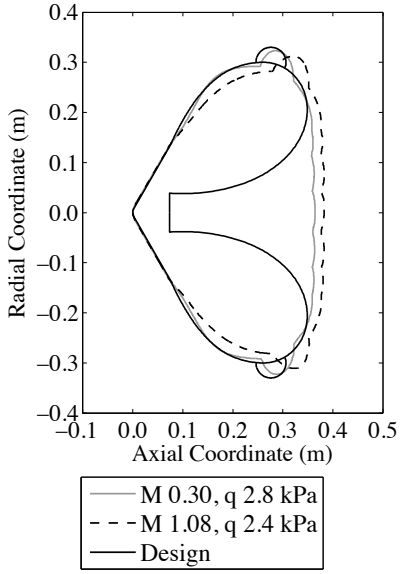

Fig. 17. Comparison of isotensoid profiles at Re 1.4M.

The subsonic isotensoid shape appears to most closely match the design shape; the transonic shape exhibits considerable axial and radial deformation. Given that the decelerator envelope was designed to a supersonic pressure distribution [9] it is not surprising that the design and actual shapes are different.

Fig. 18 illustrates the isotensoid envelope at 0° and 9° angle of attack. Note that the isotensoid envelope tries to remain aligned with the oncoming flow. In Fig. 18(b), the envelope is making contact with a significant portion of the sting adapter and balance. It is likely that the isotensoid envelope shape observed in Fig. 18(b) would not be the shape taken if the isotensoid were attached to a free-flying entry vehicle. This shape would depend on where the rear portion of the isotensoid envelope was attached to the free-flying entry vehicle.

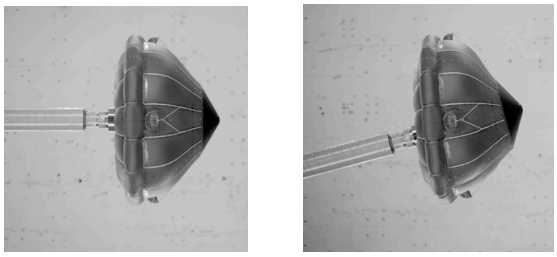

(a) 0° AoA (b) 9° AoA

Fig. 18. Isotensoid orientation at angle of attack at Mach 0.75 and Re 2.0M.

4.6. Dynamic Aeroelastic Behavior

Unlike the tension cone, the isotensoid envelope only experienced small oscillations in its shape. After several hours of testing these oscillations ultimately caused a model failure at a burble fence seam. The ram-air inlets remained fully open at all times.

5. AERODYNAMIC DATABASE

With transonic and subsonic testing complete, an aerodynamic database can be constructed for each decelerator concept throughout their applicable flight regimes. Experimental data illustrating drag coefficient of both devices are shown in Fig. 19 across all relevant flight Mach numbers at 0° angle of attack.

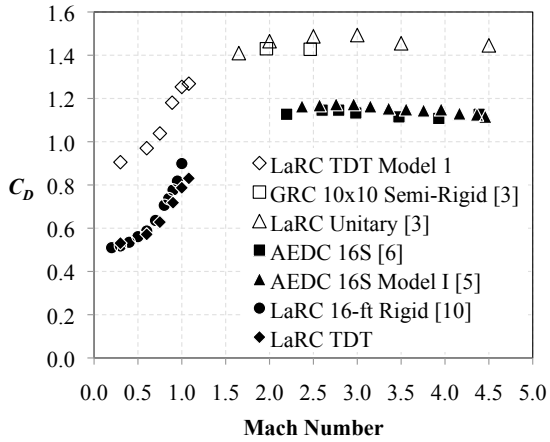

Fig. 19. Supersonic IAD drag coefficient summary, tension cone in open markers, isotensoid in solid markers. Diamonds are data from the present investigation.

These data show that the drag coefficient of the isotensoid is less than the tension cone. Although most of the isotensoid data were obtained for a 60° shape, a 70° shape was tested and exhibited only a marginal increase in drag coefficient [5], corroborating the aforementioned conclusion.

The aerodynamic data presented in Fig. 19 are useful for performing trajectory analyses of entry, descent, and landing systems during preliminary mission design.

6. SUMMARY

Inflatable aerodynamic decelerators represent a paradigm shift in decelerator technology towards devices that are attached on the perimeter of the aeroshell and can be deployed at higher Mach numbers than parachutes. System studies illustrated the benefits of landed Mars missions employing two types of supersonic IADs: the tension cone and the isotensoid. Sub-scale models of these IADs have been deployed and tested in supersonic wind tunnels to obtain quantitative data regarding their supersonic performance and behavior. Results from transonic and subsonic testing of both IADs were presented in this paper.

Both IAD geometries demonstrated smooth increase in drag through the transonic regime. The tension cone design had a greater axial force coefficient across all Mach numbers than the attached isotensoid, largely due to its shape, which is more blunt than the isotensoid. At angle of attack, the tension cone tended to remain mostly aligned with the sting. In contrast, the isotensoid tends to align itself with the flow.

The tension cone took a shape close to the desired as-designed shape. The tension cone exhibited dynamic oscillations in the pitch and yaw directions. The addition of a burble fence to the tension cone did not yield significantly improved dynamic stability. The static aeroelastic shape of the isotensoid exhibited significantly axial deformation at transonic speeds. The isotensoid envelope experienced small oscillations in its shape.

The existing knowledge base for IADs contained ample data in the supersonic regime, but was deficient in the subsonic and transonic regimes. The tests presented in this paper complete an aerodynamic database for two relevant supersonic IAD designs. This database can be used for more accurate mission analyses. These tests also provide insight into the static and dynamic behavior of supersonic IADs during mission critical events, such as ground acquisition and lander separation.

7. REFERENCES

1. Cruz, J. R. and Lingard, J. S., "Aerodynamic Decelerators for Planetary Exploration: Past, Present, and Future," AIAA Guidance, Navigation, and Control Conference and Exhibit, AIAA 2006-6792, 2006.

2. Clark, I. G., Hutchings, A. L., Tanner, C. L., and Braun, R. D., "Supersonic Inflatable Aerodynamic Decelerators for Use on Future Robotic Missions to Mars," *Journal of Spacecraft and Rockets*, Vol. 46, No. 2, March-April 2009, pp. 340-352.

3. Clark, I. G., "Aerodynamic Design, Analysis, and Validation of a Supersonic Inflatable Decelerator," Ph.D. Dissertation, Georgia Institute of Technology, August 2009.

4. Clark, I. G., Cruz, J. R., Hughes, M. F., Ware, J. S., Madlangbayan, A., Braun, R. D., "Aerodynamic and Aeroelastic Characteristics of a Tension Cone Inflatable Aerodynamic Decelerator," AIAA Aerodynamic Decelerator Systems Technology Conference and Seminar, AIAA-2009-2967, April 2000.

5. Bohon, H. L., Sawyer, J. W., and Miserentino, R., "Deployment and Performance Characteristics of 1.5-m Supersonic Attached Inflatable Decelerators," NASA TN D-7550, July 1974.

6. Bohon, H. L. and Miserentino, R., "Deployment and Performance Characteristics of 1.5-m Attached Inflatable Decelerators from Mach 2.2 to 4.4," NASA TN D-5840, August 1970.

7. Anderson, M. S., Robinson, J. C., Bush, H. G., and Fralich, R. W., "A Tension Shell Structure for Application to Entry Vehicles," NASA TN D-2675, March 1965.

8. Houtz, N. E., "Optimization of Inflatable Drag Devices by Isotensoid Design," AIAA Annual Meeting, AIAA 1964-437, June 1964.

9. Barton, R., "Development of Attached Inflatable Decelerators for Supersonic Application," NASA CR-66613, May 1968.

10. Whitcomb, C. F. and Sawyer, J. W., "Subsonic and Transonic Pressure Distributions Around a Bluff Afterbody in the Wake of a 120-degree Cone for Various Separation Distances," NASA TN D-6569, November 1971.